Direct numerical simulation of backward-facing step turbulent flow controlled by wave-machine-like traveling wave

Junichi Morita, Ryuichi Kimura, Hiroya Mamori,* and Takeshi Miyazaki
Department of Mechanical and Intelligent Systems Engineering,
The University of Electro-Communications, 1-5-1, Chofugaoka, Chofu, Tokyo 182-8585, Japan

(Received 7 March 2023; accepted 10 April 2024; published 2 May 2024)

A direct numerical simulation of turbulent flow over a backward-facing step is performed at Reynolds number of $Re_b = 5600$ based on inflow bulk velocity and channel half-width at the inlet, with an expansion ratio of ER = 1.2. To control the flow separation, a wall-normal body force in the form of a wave-machine-like traveling wave, which has streamwise and spanwise periodicity, is applied to the top surface of the step. To clarify the effect of spanwise periodicity on the reattachment length, spanwise-uniform traveling waves (SUTW) and wave-machine-like traveling waves (WMTW) are compared. The maximum reduction rates of the reattachment length in SUTW and WMTW are 51.4% and 58.9%, respectively. SUTW and WMTW exhibit a common flow behavior, in which the recirculation bubble is periodically released in time and in the streamwise direction, contributing significantly to the reduction of the reattachment length. However, spanwise periodicity produces differences in the flow structure. In SUTW, all flow structures become spanwise-uniform. In WMTW, a pair of longitudinal vortices is generated above the step and in the recirculation bubble and the released separation bubble. The pair of longitudinal vortices causes three effects that reduce the reattachment length—a decrease in the streamwise length of the secondary bubble, an enhancement of the negative wall-normal velocity, and an increase in Reynolds shear stress.

DOI: 10.1103/PhysRevFluids.9.053903

I. INTRODUCTION

Flow separation due to abrupt changes in geometry occurs in many practical applications in fluid engineering. This phenomenon leads to high form drag in aircraft, road transport vehicles, and pipes with abrupt expansions and curves. However, it promotes fuel and heat mixing in combustor. Therefore, it is crucial to develop a physical understanding of the characteristics of flow separation. Among the separated flows, the backward-facing step (BFS) flow has been frequently examined in experiments and numerical simulations because of its simple geometry as follows: the separation point is fixed at the downstream end of the BFS; only single recirculation bubble attached to that end is generated; and after reattachment, velocity profile is recovered to that of the channel flow. Thus, this flow is too simple to be considered for industrial applications, but is ideal for investigating the basic structure in flow separation.

In the 1970s $\sim$ 1990s many experiments on BFS flow were conducted. Specifically, the width of the separation region (i.e., the reattachment length) has been extensively studied, and Kuehn [1] and Ötügen [2] showed that the reattachment length increases with the expansion ratio (i.e., the height ratio of inlet to outlet in the BFS flow). Armaly *et al.* [3] showed the following relationship between Reynolds number and reattachment length: the reattachment length increases with Reynolds number

*mamori@uec.ac.jp

in laminar flows, but decreases in transitions; and the reattachment length remains relatively constant in turbulent flows. Skin-friction coefficient on the lower wall behind the BFS has been investigated by Driver and Seegmiller [4], and they found that the absolute value of the skin-friction coeffecient increased in the recirculation region. Bradshaw and Wong [5] focused on the flow profile in the recovery region and reported that the mean streamwise velocity profile does not fully recover until 50 times the step height from the separation point.

In recent decades, computer performance has improved dramatically, which has led to numerical studies on the BFS turbulent flow requiring a substantial amount of computational resources. The first direct numerical simulation (DNS) of a fully turbulent BFS was performed by Le *et al.* [6]. The results are in good agreement with experimental data reported by Jovic and Driver [7] at Reynolds number of $\mathrm{Re_h} = 5100$, defined by the step height and inflow velocity, and expansion ratio of $\mathrm{ER} = 1.2$. Barri *et al.* [8] used the cost-effective method [9] to generate realistic turbulent flow as the inlet conditions and conducted the DNS of the BFS turbulent flow at $\mathrm{Re_h} = 5600$ and $\mathrm{ER} = 2$. Here, the cost-effective method validated for DNS of the wall-bounded flow by Barri *et al.* [9] is a method that reduces computational cost by recycling a finite-length time series of instantaneous velocity planes obtained in the pre-processing simulations. The statistics upstream of the separation point are consistent with the results in DNS of the turbulent channel flow simulated by Kim *et al.* [10], and the statistics downstream of the separation point are agreement with the PIV data obtained by Kasagi and Matsunaga [11]. Thus, these two results indicate that the cost-effective method [9] is useful for inlet conditions of the BFS flow. However, many previous numerical studies, such as Le *et al.* [6], Barri *et al.* [8], Schäfer *et al.* [12], and Biswas *et al.* [13] targeted flows at low Reynolds numbers. Recently, DNS at high Reynolds numbers $\mathrm{Re}_\tau = 395$ have been performed by Pont–Vilchez *et al.* [14].

Despite numerous experiments and numerical simulations conducted to investigate the characteristics of flow separation, there is a need for applying these findings to control the flow separation in the field of fluid engineering. Chun and Sung [15] controlled the reattachment length in the BFS flow using a sinusoidal oscillating jet from a thin slit located close to the separation point. The experiment produced large vortices in the shear layer, which led to a reduction in the reattachment length. Furthermore, Wengle *et al.* [16] performed experiment and DNS of a low-amplitude time-periodic blowing and suction through a narrow slot installed at the edge of the step and investigated the effect on the reattachment length. Dahan *et al.* [17] performed a large-eddy simulation (LES) of the feedback control in spanwise-uniform slot jet and reported an increase in base pressure (i.e., reduction of form drag).

Therefore, the usefulness of time-periodic oscillations for separation flow has been demonstrated in many studies. In light of this, we focused on a traveling wave control that exhibits temporal and spatial periods. The first DNS for traveling wave control was conducted by Min *et al.* [18]. They adapted blowing and suction in the form of a traveling wave for the turbulent channel flow and realized a drag reduction rate of 30%. Since then, various effects of the traveling wave control have been actively investigated. Hœpffner and Fukagata [19] described the pumping effect as a drag reduction mechanism. Lee *et al.* [20] reported the stabilization effect of flows, and Mamori *et al.* [21] and Koganezawa *et al.* [22] showed the relaminarization effect of the turbulent flow. The heat transfer effect was investigated by Uchino *et al.* [23] and dissimilar effect between momentum and heat transfer was confirmed by Yamamoto *et al.* [24].

In our previous study (Morita *et al.* [25]), the DNS of the traveling wave control in BFS turbulent flow was performed. The control input is a wall-normal body force in the form of a spanwise-uniform traveling wave based on Mamori and Fukagata [26], which is installed above the top surface of the step. This control reduced the reattachment length by periodically releasing recirculation bubbles as a similar effect to Chun and Sung [15]. Furthermore, they reported that the turbulence generated above the step has the effect of additional reattachment length reduction. As an extension to the aforementioned study by Morita *et al.* [25], we focused on the streamwise traveling wave with a spatial periodicity in spanwise direction as well as in the streamwise direction, the so-called wave-machine-like traveling waves proposed by Nabae *et al.* [27]. The spatial periodicity in the

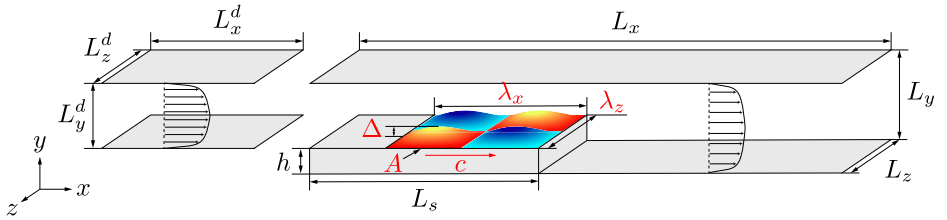

FIG. 1. Schematic view of the computational domain and traveling wave control (control parameters are colored in red).

spanwise direction is expected to enhance turbulence above the step and in the recirculation region to realize further reattachment length reduction.

In this study, we performed the DNS of the BFS turbulent flow controlled by the body force in the form of wave-machine-like traveling waves above the top surface of the step. We aimed to investigate the effects of wavespeed and spanwise wavelength in the control parameter on reattachment length. To clarify the mechanism of reattachment length reduction by the spanwise periodicity, wave-machine-like traveling wave control and spanwise-uniform traveling wave control reported in our previous study [25] were compared.

II. DIRECT NUMERICAL SIMULATION

A. Governing equations

The governing equations are the continuity and Navier–Stokes equations for incompressible flow as follows:

$$\frac{\partial u_i}{\partial x_i} = 0, \tag{1}$$

$$\frac{\partial u_i}{\partial t} + u_j \frac{\partial u_i}{\partial x_j} = -\frac{\partial p}{\partial x_i} + \frac{1}{\mathrm{Re_b}} \frac{\partial^2 u_i}{\partial x_j^2} + f_i. \tag{2}$$

Here, x_i and u_i ($i = 1 \sim 3$) denote the coordinate and velocity in the streamwise, wall-normal, and spanwise directions, respectively. Furthermore, t denotes time, p denotes pressure, and f_i denotes the body force term. The bulk Reynolds number $\mathrm{Re_b} = 2u_b^* \delta^* / \nu^*$ is 5600, where δ^* is the channel half-width at the inlet, $2u_b^*$ is the inflow bulk velocity, and ν^* denotes the kinematic viscosity. This corresponds to the friction Reynolds number $\mathrm{Re}_\tau = u_\tau^* \delta^* / \nu^* \approx 180$. Here, u_τ^* denotes the friction velocity and the asterisk denotes the dimensional variable. The flow is derived by the constant flow rate condition.

B. Computational domain

Figure 1 shows the schematic view of the computational domain and control. The computational domain consists of two parts: the driver part is the fully developed turbulent channel flow that generates the inflow of the main part; the main part is the BFS turbulent flow, and above this step the traveling wave control is applied.

The computational domain and number of the grid points for both parts are shown as Case Ref. in Table I. Here, $\mathrm{ER} = L_y/(L_y - h)$ is the expansion ratio. For both parts, the staggered grid system (Harlow *et al.* [28]) is employed and grid spacing is nonuniform along the y direction and uniform along the x and z directions. The grid resolutions in x, y, and z direction are $\Delta x^{d+} = \Delta x^+ = 4.42$, $\Delta y^{d+} = 0.932 \sim 5.97$ and $\Delta y^+ = 0.574 \sim 5.97$, and $\Delta z^{d+} = \Delta z^+ = 4.42$, respectively. The superscript $+$ denotes the wall unit and superscript d denotes the physical quantity of the driver part.

TABLE I. Computational domain and grid points.

	Driver part					Main part	
	$L_x^d \times L_y^d \times L_z^d$	$N_x^d \times N_y^d \times N_z^d$	ER	h	L_s	$L_x \times L_y \times L_z$	$N_x \times N_y \times N_z$
Kim *et al.* [10]	$4\pi \times 2 \times 2\pi$	$192 \times 129 \times 160$	—	—	—	—	—
Barri *et al.* [8]	—	—	2.0	2.0	12	$76 \times 4 \times 4\pi$	$864 \times 256 \times 200$
Case val.	$2\pi \times 2 \times 4\pi$	$128 \times 96 \times 256$	2.0	2.0	12	$76 \times 4 \times 4\pi$	$1368 \times 192 \times 256$
Case Ref.	$2\pi \times 2 \times \pi$	$256 \times 96 \times 128$	1.2	0.4	3π	$7\pi \times 2.4 \times \pi$	$896 \times 128 \times 128$
x-large	$4\pi \times 2 \times \pi$	$512 \times 96 \times 128$	1.2	0.4	6π	$14\pi \times 2.4 \times \pi$	$1792 \times 128 \times 128$
z-large	$2\pi \times 2 \times 2\pi$	$256 \times 96 \times 256$	1.2	0.4	3π	$7\pi \times 2.4 \times 2\pi$	$896 \times 128 \times 256$
x-fine	$2\pi \times 2 \times \pi$	$512 \times 96 \times 128$	1.2	0.4	3π	$7\pi \times 2.4 \times \pi$	$1792 \times 128 \times 128$
y-fine	$2\pi \times 2 \times \pi$	$256 \times 192 \times 128$	1.2	0.4	3π	$7\pi \times 2.4 \times \pi$	$896 \times 256 \times 128$
z-fine	$2\pi \times 2 \times \pi$	$256 \times 96 \times 256$	1.2	0.4	3π	$7\pi \times 2.4 \times \pi$	$896 \times 128 \times 256$

C. Boundary conditions and computational schemes

As the boundary condition in the driver part, a periodic condition is imposed in x and z directions, and no-slip condition is imposed on the wall. For the main part, the periodic boundary condition is applied in z direction. The no-slip condition is imposed on the wall and BFS is represented using the immersed boundary method proposed by Kim *et al.* [29].

Inflow conditions have a significant impact on the flow structure downstream of the separation point. Hence, a time-dependent and three-dimensional spatial turbulence that satisfies the continuity equation and momentum balance must be reproduced at the inlet. Therefore, in the present simulation, driver and main parts are simulated synchronously such that the inflow velocity in the main part is updated every time step with the velocity distribution of the fully developed turbulent channel flow obtained from certain y-z plane of the driver part. For this, the width and grid resolutions in the y-z plane at the inlet of the main part are consistent with those of the driver part. The outlet condition is the convection condition as follows:

$$\frac{\partial u_i}{\partial t} + U_c \frac{\partial u_i}{\partial x} = 0, \tag{3}$$

where U_c is the convection velocity at the outlet.

The computational schemes in the DNS code are based on the turbulent channel flow described by Fukagata *et al.* [30]: the governing equations are spatially discretized using an energy conservative second-order accurate central finite difference method (Ham *et al.* [31]). The time advancement scheme is the second-order Crank–Nicolson scheme for viscosity terms and the low-storage third-order Runge–Kutta scheme for other terms. These schemes are combined with the simplified marker and cell method (Dukowicz*et al.* [32]) as the coupling of the velocity and pressure.

D. Control method

As shown in Fig. 1, the body force control in the form of a wave-machine-like traveling wave is applied on the top surface of step. The control range is $\pi < x < 3\pi$ to prevent interference between the inflow and control. Given that the body forces are assumed to exponentially decay in the wall-normal direction [26], the control equation is expressed as follows:

$$f_x = f_z = 0, \tag{4}$$

$$f_y = A \exp\left(-\frac{y-h}{\Delta}\right) \sin\left(\frac{2\pi}{\lambda_x}(x - ct)\right) \sin\left(\frac{2\pi}{\lambda_z} z\right) \qquad \begin{matrix}(\pi \leqslant x \leqslant 3\pi) \\ (h \leqslant y \leqslant h + \Delta),\end{matrix} \tag{5}$$

where control parameters are amplitude A, penetration length Δ, streamwise wavelength λ_x, spanwise wavelength λ_z, and wavespeed c.

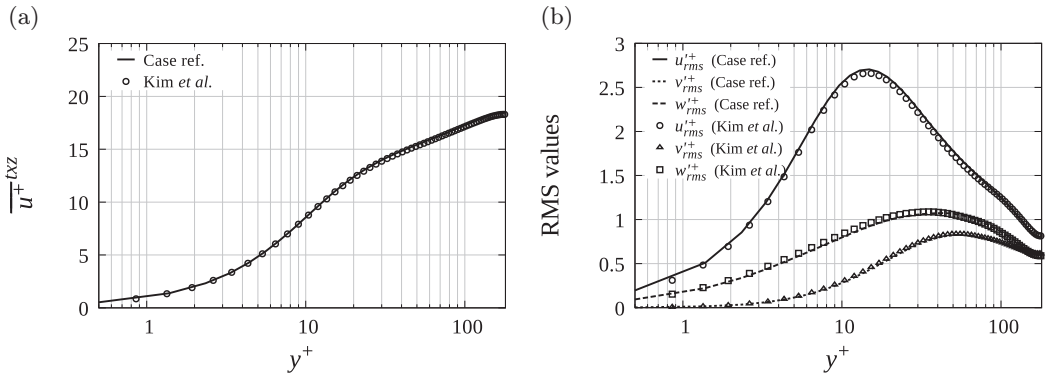

FIG. 2. Flow statistics in the driver part: (a) mean streamwise velocity profile; (b) RMS values of streamwise, wall-normal, and spanwise velocity ($u'^+_{i,\mathrm{rms}} = \sqrt{\overline{u_i'^+ u_i'^+}^{txz}}$).

In this study, the unique effects of wave-machine-like traveling waves were thoroughly examined by comparing them to the effects of spanwise-uniform traveling waves. Here, when the spanwise wave number is $k_z = 2\pi/\lambda_z = 0$, the control input is a spanwise-uniform traveling wave, and when $k_z \geqslant 1$, the control input is a wave-machine-like traveling wave. Hereafter, spanwise-uniform traveling waves are denoted as SUTW, and wave-machine-like traveling waves are denoted as WMTW. All simulations start from the fully developed turbulent channel flow and BFS turbulent flow, and the control start time is set to $t = 0$.

To evaluate the control effect in detail, phase average is used, which is defined for an arbitrary physical quantity g as follows:

$$\langle g \rangle(x, y, \phi_z, \phi_t) = \frac{1}{N_{\phi_z} N_{\phi_t}} \sum_{z \in \phi_z} \sum_{t \in \phi_t} g(x, y, z, t), \tag{6}$$

where $\phi_z = z - m\lambda_z$ $(0 \leqslant \phi_z \leqslant \lambda_z, m \in \mathbb{Z})$ and $\phi_t = t - nT$ $(0 \leqslant \phi_t \leqslant T, n \in \mathbb{Z})$ are the coordinate within one period of the spanwise wave and time within traveling wave one period $T = \lambda_x/|c|$, respectively. Additionally, N_{ϕ_z} is the unit number of the spanwise wave in the computational domain and N_{ϕ_t} denotes total number of time-series data used for phase average.

E. Validation and verification

Table I shows the different conditions used for validation and verification. First, the results corresponding to Case Ref. and Kim *et al.* [10] were compared to validate the driver part (i.e., the fully developed turbulent channel flow). Figure 2 shows the mean streamwise velocity profile and RMS values of velocity in x, y, and z directions. Here, the bar and prime are the mean value and deviation, respectively, as follows:

$$u_i = \overline{u_i}^{txz} + u_i', \tag{7}$$

where superscript t, x, and z denote mean average in time, x, and z directions, respectively. Evidently, the results of the present simulation are in excellent agreement with those of Kim *et al.* [10].

Subsequently, to validate the main part (i.e., the BFS turbulent flow), Case val. similar to the computational conditions of Barri *et al.* [8] was employed. Here, in Barri *et al.* [8], the conditions of the driver part are not described in Table I because the cost-effective method [9] is used to generate

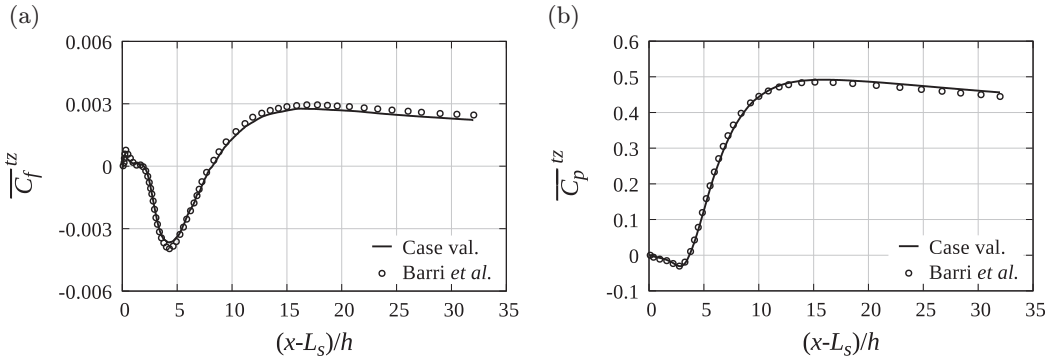

FIG. 3. Flow statistics in the main part: (a) skin-friction coefficient and (b) pressure coefficient averaged in time and z direction.

the inflow velocity of the BFS turbulent flow. Figure 3 shows the skin-friction coefficient $\overline{C_f}^{tz}$ and pressure coefficient $\overline{C_p}^{tz}$ averaged in time and z direction, which are defined as follows:

$$\overline{C_f}^{tz} = \frac{\overline{\tau_w^*}^{tz}}{\frac{1}{2}\rho^*(u_b^*)^2}, \tag{8}$$

$$\overline{C_p}^{tz} = \frac{\overline{p^*}^{tz} - \overline{p_0^*}^{tz}}{\frac{1}{2}\rho^*(u_b^*)^2}. \tag{9}$$

Here, τ_w^* denotes the lower wall shear stress, ρ^* denotes the density, and p_0^* denotes the lower wall pressure at the downstream edge of step $x = L_s$. The horizontal axis is normalized by step height h, and origin $(x - L_s)/h = 0$ corresponds to the downstream edge of the step. The results of present simulations and Barri *et al.* [8]. are in good agreement. Hence, the present DNS code can reproduce the BFS turbulent flow.

Finally, we verified the computational domain size and grid resolution. The following six computational conditions are used as shown in Table I: x-large and z-large have larger domains as compared with Case ref., and x-fine, y-fine, and z-fine exhibit higher grid resolution. Figure 4 shows the skin-friction coefficient and pressure coefficient averaged in time and z direction in the uncontrolled case and control case. In the control case, the control parameter is fixed at $A = 2$, $\Delta = 0.1$, $\lambda_x = 2\pi$, $\lambda_z = \pi$, and $c = 0.4$. Since the differences in each domain and grid resolution are extremely small, Case Ref. is used in the simulation in Sec. III.

III. RESULTS AND DISCUSSION

In this section, only the data in statistical equilibrium state are discussed to accurately evaluate the effect on the reattachment length and clarify its reduction mechanism in WMTW and SUTW.

Figure 5(a) shows the skin-friction coefficient averaged in time and z direction in the w/o control. The definitions of the horizontal axis and origin are the same as those in Fig. 3. Near the separation point $0 \leqslant (x - L_s)/h \leqslant 2.36$, $\overline{C_f}^{tz}$ is slightly positive, which corresponds to the secondary bubble generated by the recirculation bubble. Conversely, in the range of $2.36 \leqslant (x - L_s)/h \leqslant 6.25$, $\overline{C_f}^{tz}$ decreases significantly because of the backflow in the recirculation bubble. After reattachment, $\overline{C_f}^{tz}$ gradually recovers downstream. Thus, the definition of the reattachment length is the distance from the origin (i.e., the separation point) to the third $\overline{C_f}^{tz} = 0$ point (i.e., reattachment point).

Figure 5(b) shows the effect of WMTW and SUTW on the reattachment length as a function of wavespeed. Here, the marker denotes single computational run of the control cases and only the spanwise wavelength $\lambda_z = \pi$ is plotted in the WMTW. The other fixed parameters are $A = 2$,

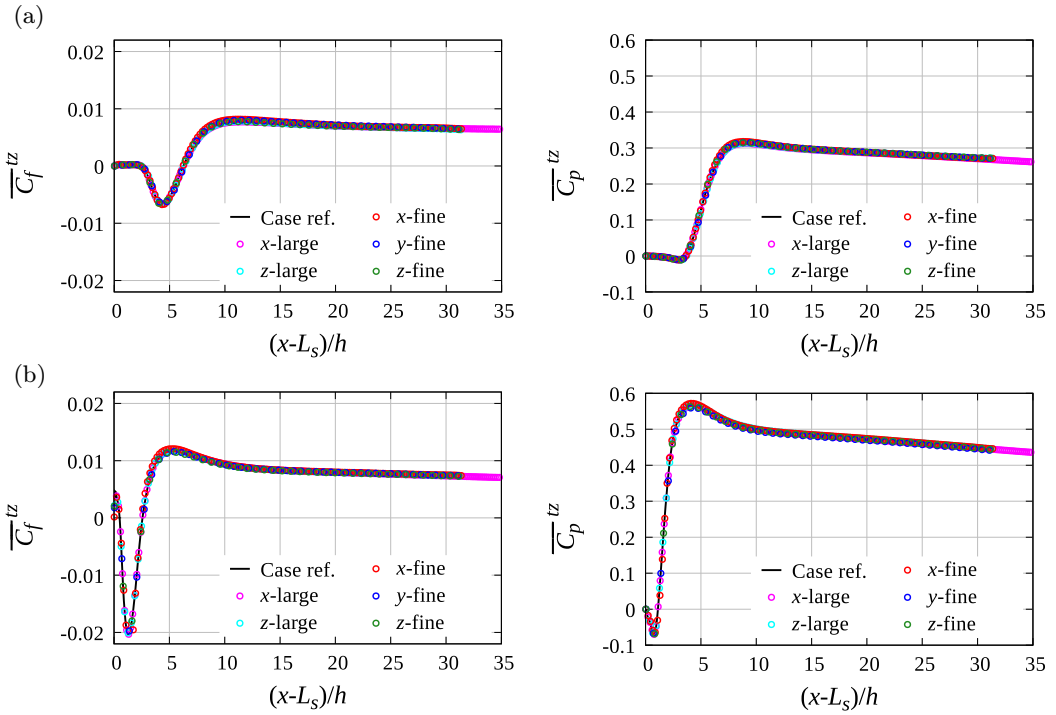

FIG. 4. Skin-friction coefficient (left) and pressure coefficient (right) averaged in time and z direction: (a) w/o control; (b) controlled.

$\Delta = 0.1$, and $\lambda_x = 2\pi$. In all control cases, the reattachment length is reduced as compared to w/o control. At $|c| \geqslant 1.5$, the reattachment lengths are similar in both control cases. However, at $|c| \leqslant 1.5$, WMTW reduces the reattachment length more than SUTW. The wavespeed that leads to the highest reduction in the reattachment length in both cases is $c = 0.4$. The minimum reattachment lengths for WMTW and SUTW are $\overline{X_r}^{tz}/h = 2.57$ and $\overline{X_r}^{tz}/h = 3.04$, respectively. Hence, given that the reattachment length in w/o control is $\overline{X_r}^{tz}/h = 6.25$, SUTW and WMTW at $c = 0.4$ realize a maximum reduction of 51.4% and 58.9% in reattachment length, respectively.

Therefore, we investigated the effect of spanwise wavelength on the reattachment length at $c = 0.4$, as shown in Figure 5(c). Here, the spanwise wavelength in SUTW corresponds to infinity. The other fixed parameters are $A = 2$, $\Delta = 0.1$, and $\lambda_x = 2\pi$. In all control cases, the reattachment length is reduced regardless of the spanwise wavelength as compared to w/o control. For the WMTW, the reattachment length decreases as the spanwise wavelength increases, and the minimum value is obtained at $\lambda_z = \pi$.

The effects of streamwise wavelength, amplitude, and penetration length are shown in Figs. 5(d)–5(f). The other fixed parameters are $A = 2$, $\Delta = 0.1$, $\lambda_x = 2\pi$, $\lambda_z = \pi$, and $c = 0.4$. The streamwise wavelength has little effect on the reattachment length, while the reattachment length decreases with increasing amplitude and penetration length. Accordingly, we chose the control parameter sets of $A = 2$, $\Delta = 0.1$, and $\lambda_x = 2\pi$. In subsequent analyses, SUTW (with $\lambda_z = \infty$) and WMTW with $\lambda_z = \pi$ are compared at $c = 0.4$.

Figure 6(a) shows the skin-friction coefficient averaged in time and z direction in WMTW and SUTW. In both control cases, the positive $\overline{C_f}^{tz}$ in the region of the secondary bubble increases significantly more than that in the w/o control. Additionally, the negative $\overline{C_f}^{tz}$ in the recirculation region is significantly reduced. Hence, the rotation of recirculation bubble is enhanced, which in

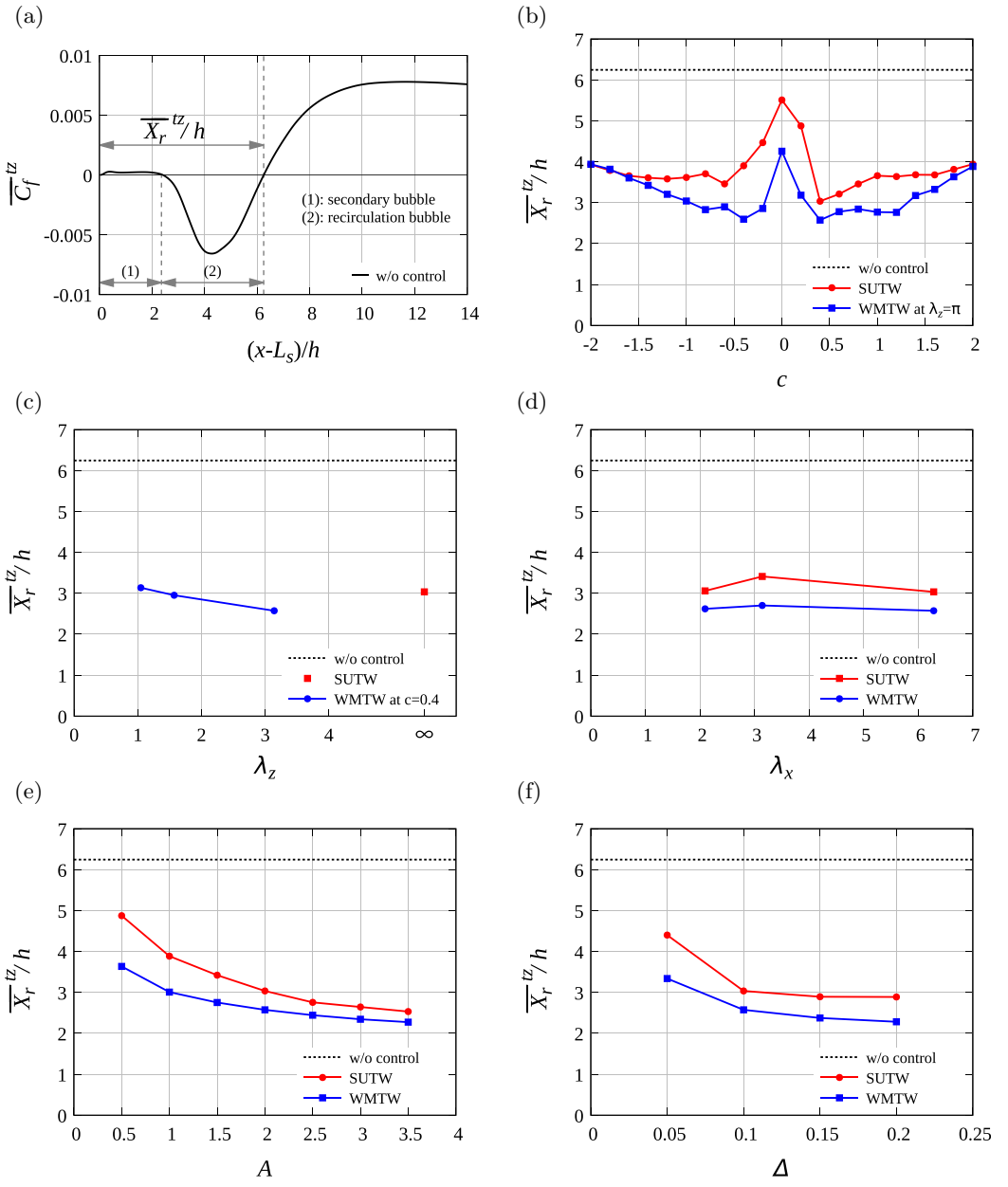

FIG. 5. Skin-friction coefficient and reattachment length: (a) definition of reattachment length determined from the skin-friction coefficient averaged in time and z direction; effect of wavespeed (b) and spanwise wavelength (c), streamwise wavelength (d), amplitude (e), and penetration length (f) on reattachment length. In (b–f), the other control parameters are fixed at $A = 2$, $\Delta = 0.1$, $\lambda_x = 2\pi$, $\lambda_z = \pi$, and $c = 0.4$.

turn also enhances the rotation of the secondary bubble. In both controls, the streamwise width of the recirculation bubble is almost the same. Conversely, the streamwise width of the secondary bubble in WMTW is shorter than that in SUTW, which reduces the reattachment length in WMTW as compared to that in SUTW.

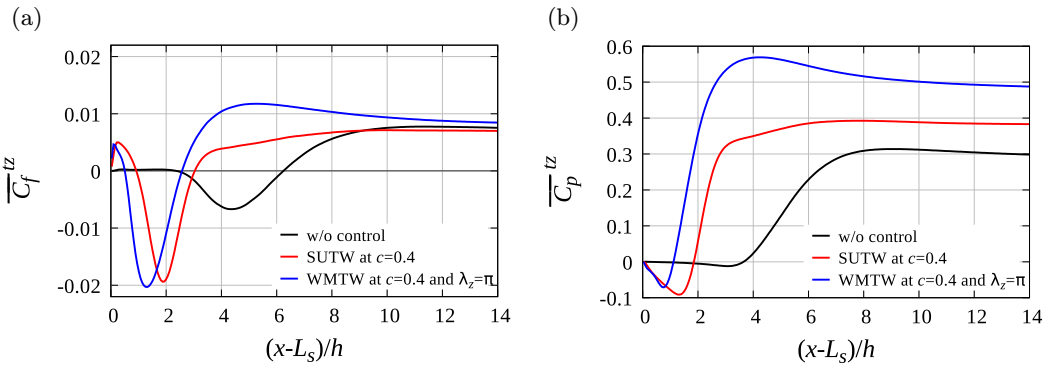

FIG. 6. Skin-friction coefficient (a) and pressure coefficient (b): black, w/o control; red, SUTW; blue, WMTW.

Figure 6(b) shows the pressure coefficient. In the controlled cases, the pressure coefficients decrease in the region of the secondary bubble, increase abruptly in the region of the separation bubble, and approach to the constant value in the recovery region. As the secondary bubble region is smaller in the WMTW than in the SUTW, pressure recovery occurs more upstream.

Figure 7 shows the wall-normal velocity averaged in time and z direction $\overline{v}^{tz}$. In WMTW, the wall-normal velocity is significantly reduced in the recirculation region and recovery region as compared to w/o control and SUTW.

Figure 8 shows the Reynolds shear stress (RSS) $\overline{u'v'}^{tz}$. In WMTW, the RSS increases significantly in the recirculation region and recovery region as compared to the other two cases.

In summary, WMTW enhances the negative wall-normal velocity and RSS in the recirculation region and recovery region as compared to the w/o control and SUTW, which directly reduce the reattachment length to highest extent. Subsequently, the mechanisms of negative wall-normal velocity and RSS enhancement are discussed.

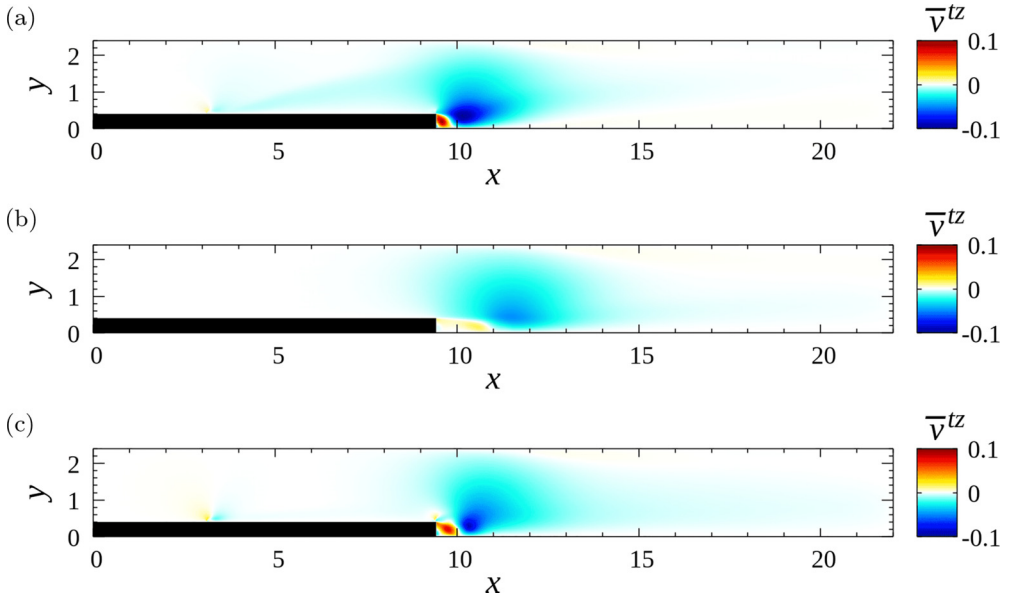

FIG. 7. Wall-normal velocity averaged in time and z direction: (a) w/o control; (b) SUTW; (c) WMTW.

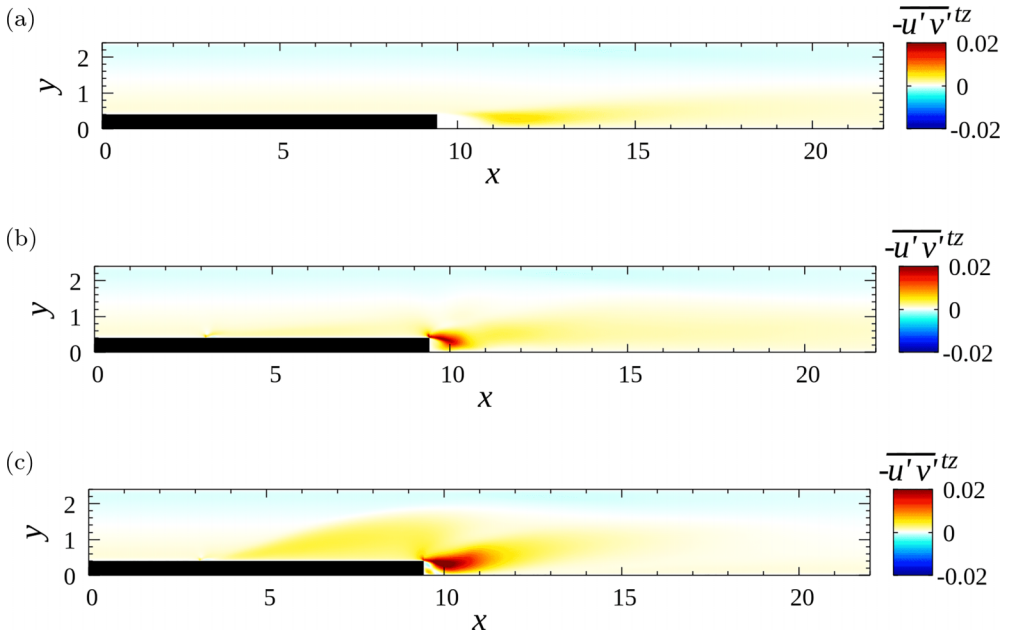

FIG. 8. Reynolds shear stress averaged in time and z direction: (a) w/o control; (b) SUTW; (c) WMTW.

Figure 9 shows the instantaneous turbulent vortical structures visualized by the second invariant of the velocity gradient tensor, the so-called Q value. The threshold for the turbulent vortical structures is $Q = 4$, and the contour shown above the step is the wall-normal body force distribution f_y at $y = 0.405$. The time corresponds to $t = t^* 2u_b^*/\delta^* = 518.4$. Here, we compare the vortical structures for four cases (SUTW at $c = 0.4$, SUTW at $c = -0.4$, WMTW at $c = 0.4$, and WMTW at $c = -0.4$) to investigate the effect of the direction of the traveling wave. In w/o control, the turbulent vortical structures are absent above the step and in the region of the secondary bubble. Conversely, they are promoted in the region of recirculation bubble and become gradually weaker toward the downstream side. In the controlled case, the turbulent vortical structures are strongly promoted above the step and in the region of recirculation bubble attached to the step. Since the recirculation bubbles are periodically released, regions without the turbulent vortical structures and regions where the turbulent vortical structures are promoted appear alternately toward the downstream side. Hereafter, to distinguish between the recirculation bubble attached to the step and released recirculation bubble, they are referred to as the recirculation bubble and released separation bubbles, respectively.

Thus, SUTW and WMTW have three things in common regardless of the direction of the traveling wave: the first is the generation of turbulent vortical structures above the step; the second is the enhancement of turbulent vortical structures in the recirculation region; the third is the periodic release of the recirculation bubbles.

The direction of the traveling wave affects the vortical structures on the step. They are strongly promoted at $c = 0.4$ and suppressed at $c = -0.4$. However, the shapes of these vortical structures differ for SUTW and WMTW. In SUTW, the shapes of the turbulent vortical structures above the step and in the recirculation region are uniform in z direction, whereas in the WMTW, they are nonuniform in z direction and are very complex. Additionally, SUTW periodically releases recirculation bubbles with axis in z direction, whereas WMTW alternately releases recirculation bubbles at $0 \leqslant z \leqslant \pi/2$ and $\pi/2 \leqslant z \leqslant \pi$. Therefore, to analyze the differences in the shape of these turbulent vortical structure in more detail, the coherent component is extracted by using the phase average.

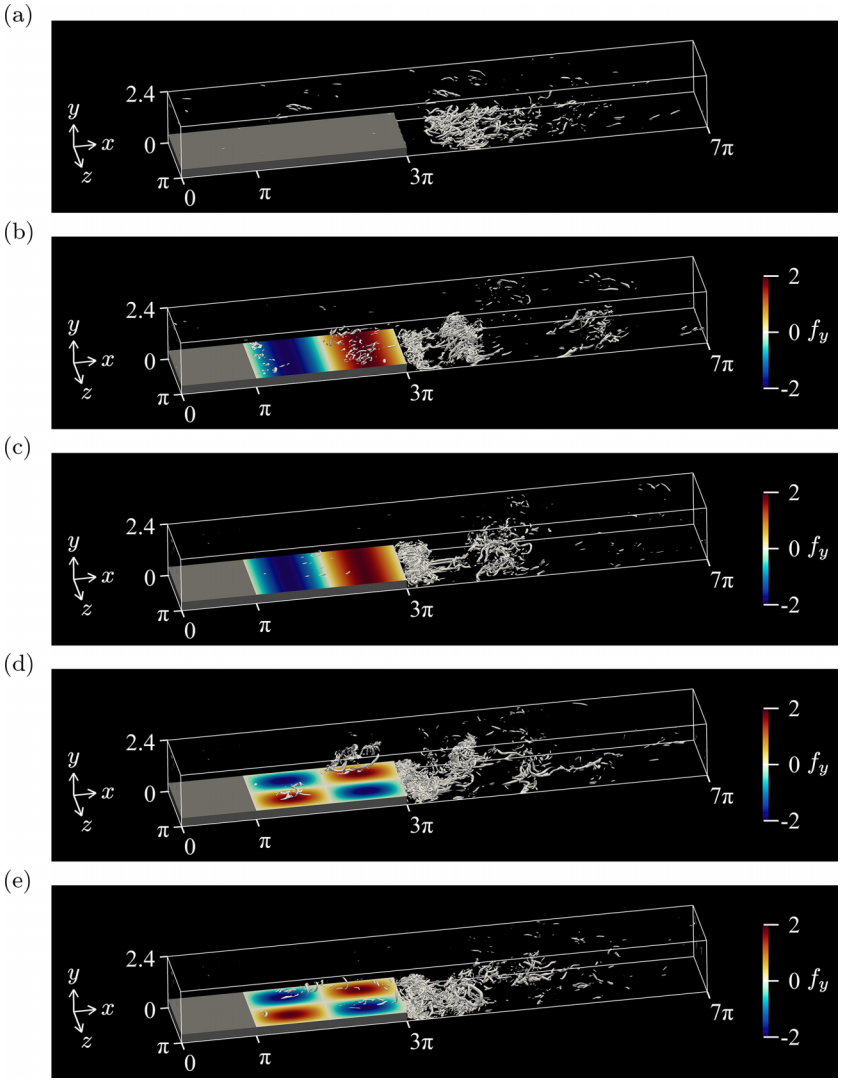

FIG. 9. Instantaneous vortical structures visualized by the second invariant of the velocity gradient tensor. The threshold is $Q = 4$, and the contour shown above the step is wall-normal body force f_y at $y = 0.405$. The time is $t = 518.4$: (a) w/o control; (b) SUTW at $c = 0.4$; (c) SUTW at $c = -0.4$; (d) WMTW at $c = 0.4$; (e) WMTW at $c = -0.4$.

Figure 10 shows the coherent component of the vortical structures by the downstream traveling wave at $c = 0.4$ in SUTW and WMTW. The structures are visualized by the second invariant of the phase-averaged velocity gradient tensor, and the threshold is $\langle Q \rangle = 0.1$. The surface of the vortical structures is colored with phase-averaged wall-normal velocity $\langle v \rangle$ to clarify the rotation axis of the vortex. Only ranges $2\pi \leqslant x \leqslant 4\pi$ and $0 \leqslant z \leqslant \pi/2$ are visualized to observe the flow structure above the step and in the separation regions in detail. In SUTW and WMTW, the behavior of the coherent component of the vortical structures are similar. At $\phi_t = 0$, the vortical structures are promoted above the step. At $\phi_t = T/4$, these vortical structures are transported to the separation point. At $\phi_t = T/2$, these vortical structures and recirculation bubble combine, and the recirculation

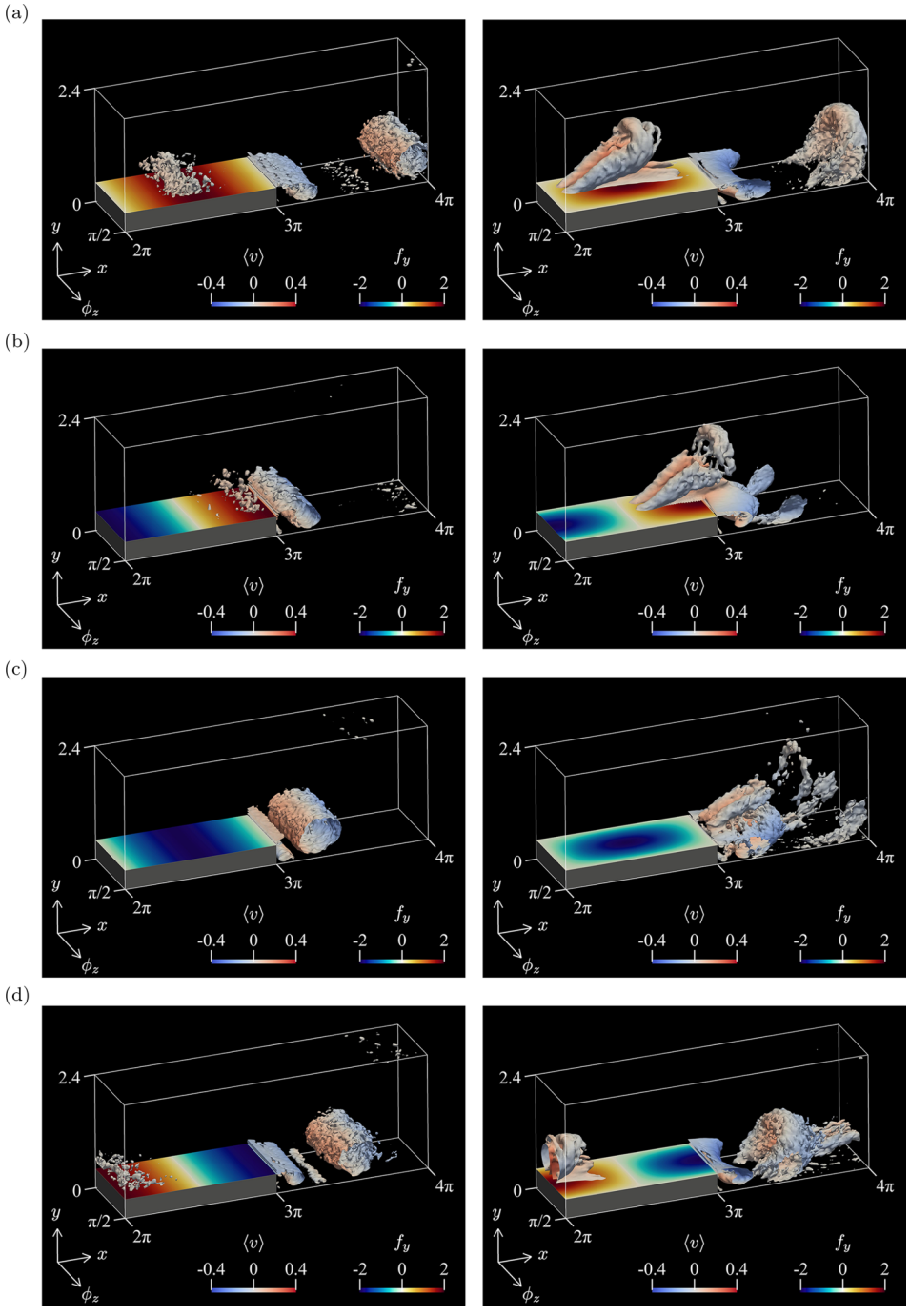

FIG. 10. Coherent component of vortical structures around the separation point. The structures are visualized by the second invariant of the phase-averaged velocity gradient tensor, and the threshold is $\langle Q \rangle = 0.1$. The contour shown above the step is wall-normal body force f_y at $y = 0.405$, and the surface of the vortical structures is colored with phase-averaged wall-normal velocities $\langle v \rangle$. Left column is SUTW at $c = 0.4$ and right column is WMTW at $c = 0.4$: (a) $\phi_t = 0$; (b) $\phi_t = T/4$; (c) $\phi_t = T/2$; (d) $\phi_t = 3T/4$.

bubble becomes larger. At $\phi_t = 3T/4$, the recirculation bubble is released and a new recirculation bubble is generated.

However, there is a significant difference in the shape of the coherent component of the vortical structures for SUTW and WMTW. In SUTW, the vortical structures generated above the step, recirculation bubble, and released separation bubbles are all spanwise-uniform. Conversely, in WMTW, the vortical structures generated above the step exhibit the shape of the pair of longitudinal vortices. The recirculation bubble is spanwise nonuniform. The released separation bubble is in the shape of the horseshoe vortex. In Fig. 12, perspectives from other directions are visualized to analyze in detail the generation mechanism of these complex vortical structures in the WMTW.

To discuss the effect of the direction of the traveling wave, Fig. 11 shows the coherent component of the vortical structures by the upstream traveling wave at $c = -0.4$ in SUTW and WMTW. In SUTW, in contrast with $c = 0.4$, the vortical structures on the step are absent. In WMTW, a pair of the vortical structures on the step is observed.

In our previous study (Morita *et al.* [25]), we concluded that the recirculation bubble is strongly influenced by the body force around the edge of the step. The effect does not depend on the direction of the traveling wave. Therefore, in WMTW and SUTW, the effects contribute to the roughly symmetrical profile of the reattachment length as shown in Fig. 5(b). However, the vortical structure generated above the step depends on the direction of the traveling wave and WMTW/SUTW, also affecting the reattachment length.

Figures 12(a) and 12(c) shows the top view of the coherent component of vortical structures in WMTW at $c = 0.4$. Here, only ranges $2\pi \leqslant x \leqslant 4\pi$ are visualized. At $\phi_t = 0$ and $\phi_t = T/4$, the recirculation bubble exhibits the shape of a spanwise sine wave. This is attributed to the fact that the behavior of $0 < z < \pi/2$ and $\pi/2 < z < \pi$ is shifted by just half a period $T/2$, which is natural because they are phase-averaged. Hence, expansion and generation of the recirculation bubble occur at $0 < z < \pi/2$ and $\pi/2 < z < \pi$ simultaneously, and the effects of expansion and generation alternate time-periodically in the z direction. For example, at $\phi_t = T/4$, the recirculation bubble becomes large at $0 < z < \pi/2$ because it is combined with the vortical structures generated above the step, whereas it becomes small at $\pi/2 < z < \pi$ because a new one is generated. Accordingly, the recirculation bubble oscillates in the form of the spanwise wave, whose wavelength is determined by the control input, λ_z.

Figures 12(b) and 12(d) shows the coherent component of vortical structures viewed from the lower wall. Here, the coordinates correspond to Figs. 12(a) and 12(c). At $\phi_t = 0$, the recirculation bubble at $\pi/2 < z < \pi$ has an axis in x direction rather than that in z direction.

There is a possible reason for this: the recirculation bubble forms a sine wave shape. At $\phi_t = T/4$, a new recirculation bubble is generated at $\pi/2 < z < \pi$, and the original recirculation bubble is released in the shape of a horseshoe vortex. Within the horseshoe vortex, there is a pair of longitudinal vortices. Therefore, the streamwise rotation of the recirculation bubble (at $\phi_t = 0$) contributes significantly to the generation of the horseshoe vortex.

Figure 13 shows the phase-averaged streamwise vorticity at the reattachment point $x = 10.46$. The two pairs of the vortices are confirmed. The far-wall vortices are the longitudinal vortices generated on the step; the near-wall vortices originate from the recirculation bubble. We found that the streamwise vorticity $\langle \omega_z \rangle$ of the recirculation bubble is much greater than that of longitudinal vortices.

Figure 14 shows the coherent component of the vortical structures. At $\phi_t = T/2$, the recirculation bubble combines with the longitudinal vortices generated above the step. The pair of the longitudinal vortices has already been generated within the recirculation bubble. These are due to the fact that the recirculation bubble is deformed into the sine wave shape at $\phi_t = T/4$. As shown in Fig. 13, the rotation of the longitudinal vortices within the recirculation bubble is much larger than that of the vortices generated above the step. At $\phi_t = 3T/4$, the downward flow is induced around the edge of the step, which releases the recirculation bubble. The released recirculation bubble develops a horseshoe vortex.

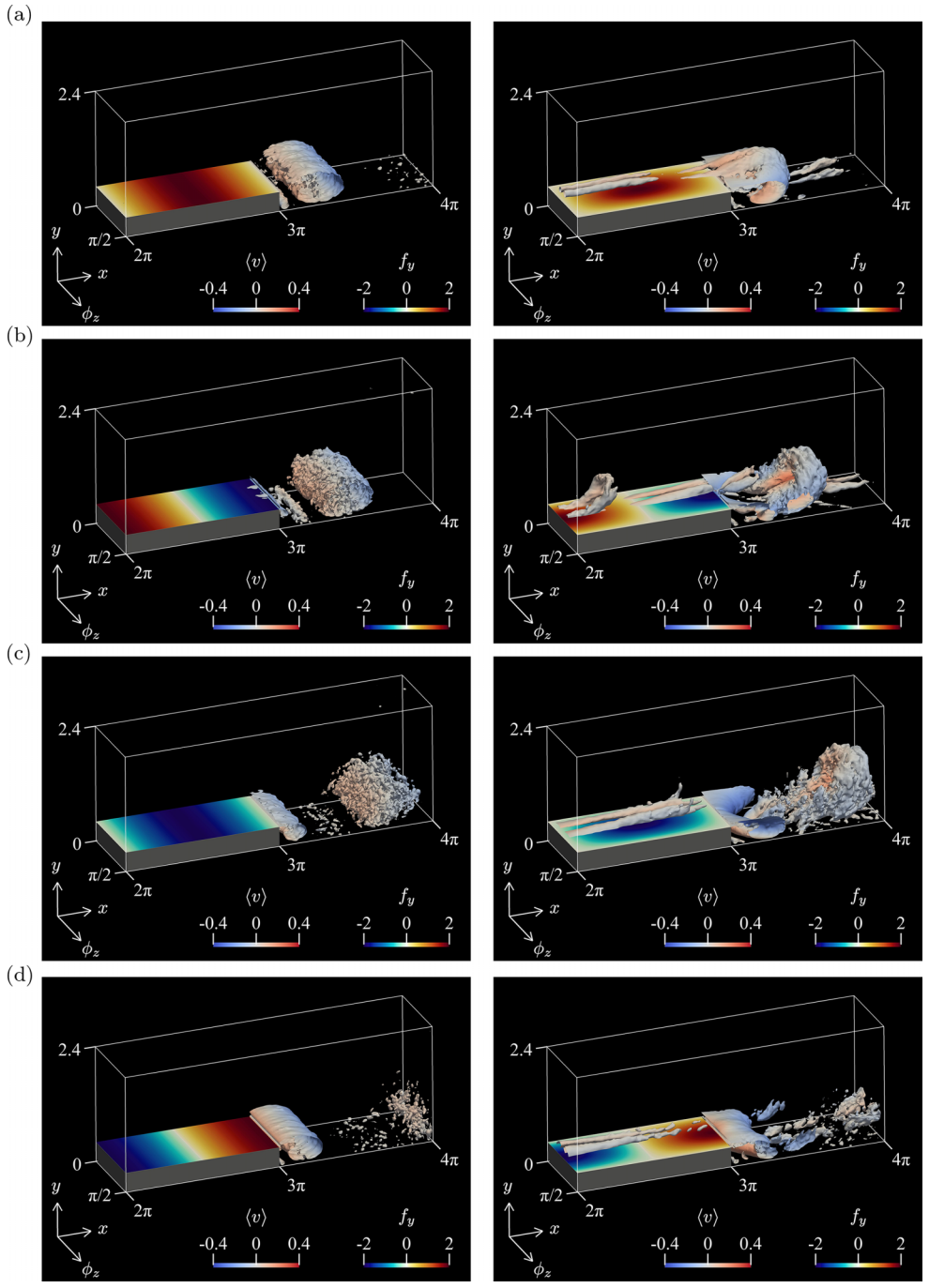

FIG. 11. Coherent component of vortical structures around the separation point. The structures are visualized by the second invariant of the phase-averaged velocity gradient tensor, and the threshold is $\langle Q \rangle = 0.1$. The contour shown above the step is wall-normal body force f_y at $y = 0.405$, and the surface of the vortical structures is colored with phase-averaged wall-normal velocities $\langle v \rangle$. Left column is SUTW at $c = -0.4$ and right column is WMTW at $c = -0.4$: (a) $\phi_t = 0$; (b) $\phi_t = T/4$; (c) $\phi_t = T/2$; (d) $\phi_t = 3T/4$.

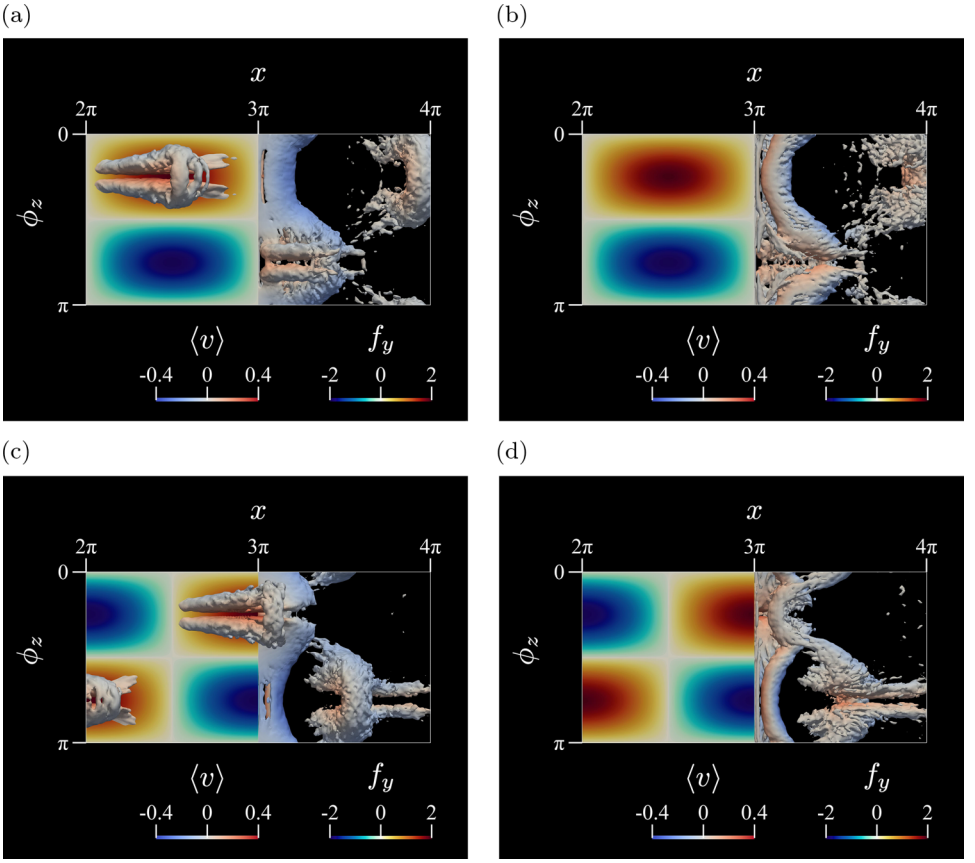

FIG. 12. Coherent component of vortical structures around the separation point in WMTW at $c = 0.4$. The structures are visualized by the second invariant of the phase-averaged velocity gradient tensor, and the threshold is $\langle Q \rangle = 0.1$. The contour shown above the step is wall-normal body force f_y at $y = 0.405$, and the surface of the vortical structures is colored with phase-averaged wall-normal velocities $\langle v \rangle$. Left column is top view and right column is viewed from the lower wall: (a, b) $\phi_t = 0$; (c, d) $\phi_t = T/4$.

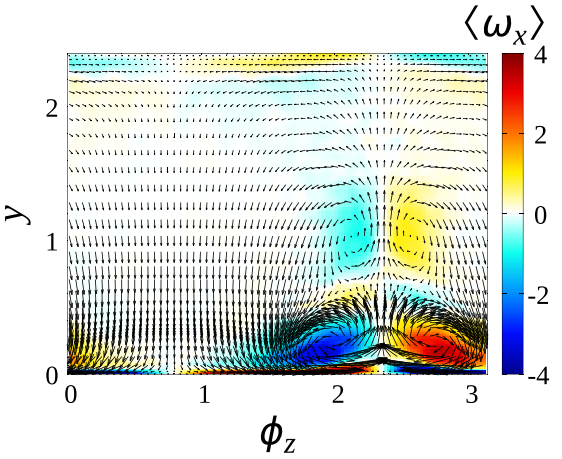

FIG. 13. Phase-averaged streamwise vorticity at $\phi_t = 0$ and $x = 10.46$ in WMTW with $c = 0.4$. Arrows are the phase-averaged velocity vector of $\langle w \rangle$ and $\langle v \rangle$.

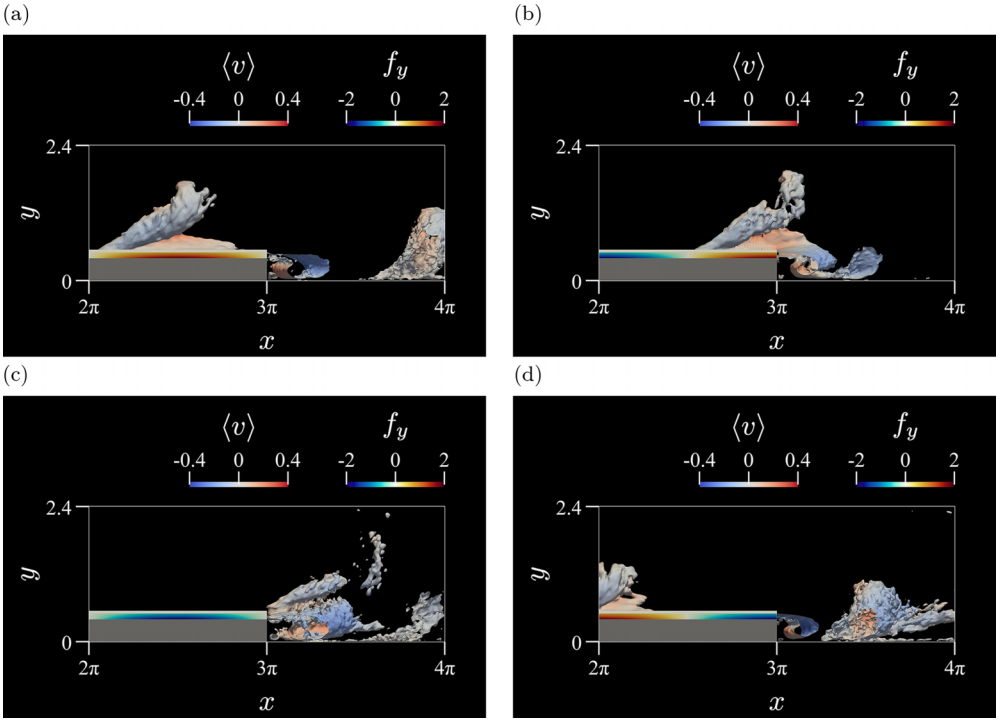

FIG. 14. Coherent component of vortical structures around the separation point in WMTW with $c = 0.4$. The structures are visualized by the second invariant of the phase-averaged velocity gradient tensor, and the threshold is $\langle Q \rangle = 0.1$. The contour shown above the step is wall-normal body force f_y, and the surface of the vortical structures is colored with phase-averaged wall-normal velocities $\langle v \rangle$. The structures are viewed from spanwise direction: (a) $\phi_t = 0$; (b) $\phi_t = T/4$ (c) $\phi_t = T/2$; $(d)\phi_t = 3T/4$.

Figure 15 shows the time trace of the reattachment length $X_r(z,t)/h$ at $z = \pi/4$ and $\pi/2$. Here, the reattachment length $X_r(z,t)/h$ is obtained from the skin-friction coefficient $C_f(x,z,t)$. In addition, $z = \pi/4$ and $\pi/2$ correspond to the antinode and node of WMTW in the spanwise direction. In the w/o control case, the reattachment length shows multiple oscillation frequencies due to the effect of the turbulent vortical structures. In contrast, at SUTW, the variation of reattachment length is strongly affected by a single frequency consisting of a traveling wave period $T = \lambda/c = 15.7$. In particular, the coherent component of the vortical structure generated by the traveling wave dominates the expansion and release of the recirculation bubbles. In WMTW, the reattachment length at $z = \pi/4$ is similar to SUTW and the period corresponds to that of the traveling wave. However, at $z = \pi/2$, the frequency increases compared to those at $z = \pi/4$. Thus, at the antinode of WMTW, the coherent component dominates the expansion and release of the recirculation bubbles; at the node, the turbulent vortical structure also affects them.

Figure 16 shows the variation of the phase-averaged reattachment length in SUTW and WMTW. They are obtained from the phase-averaged skin-friction coefficient $\overline{\langle C_f \rangle}^z(x, \phi_t)$ and $\langle C_f \rangle(x, \phi_z, \phi_t)$, respectively. Here, SUTW is homogeneous in the z direction and is therefore averaged in the z direction. In the WMTW, $\phi_z = \lambda_z/4$ and $\phi_z = 3\lambda_z/4$ correspond to the antinode in the spanwise wave of the control input and $\phi_z = \lambda_z/2$ corresponds to the node. In SUTW, the reattachment length increases gradually and decreases rapidly, which corresponds to the expansion and generation/release of the recirculation bubbles, respectively. In WMTW, at $\phi_z = \lambda_z/4$ and $3\lambda_z/4$, the variation in the reattachment length is very similar to that of SUTW, but its oscillation width is slightly smaller. In the three cases, the dominant frequency is $f = |c|/\lambda_x = 0.064$ because the streamwise wavelength

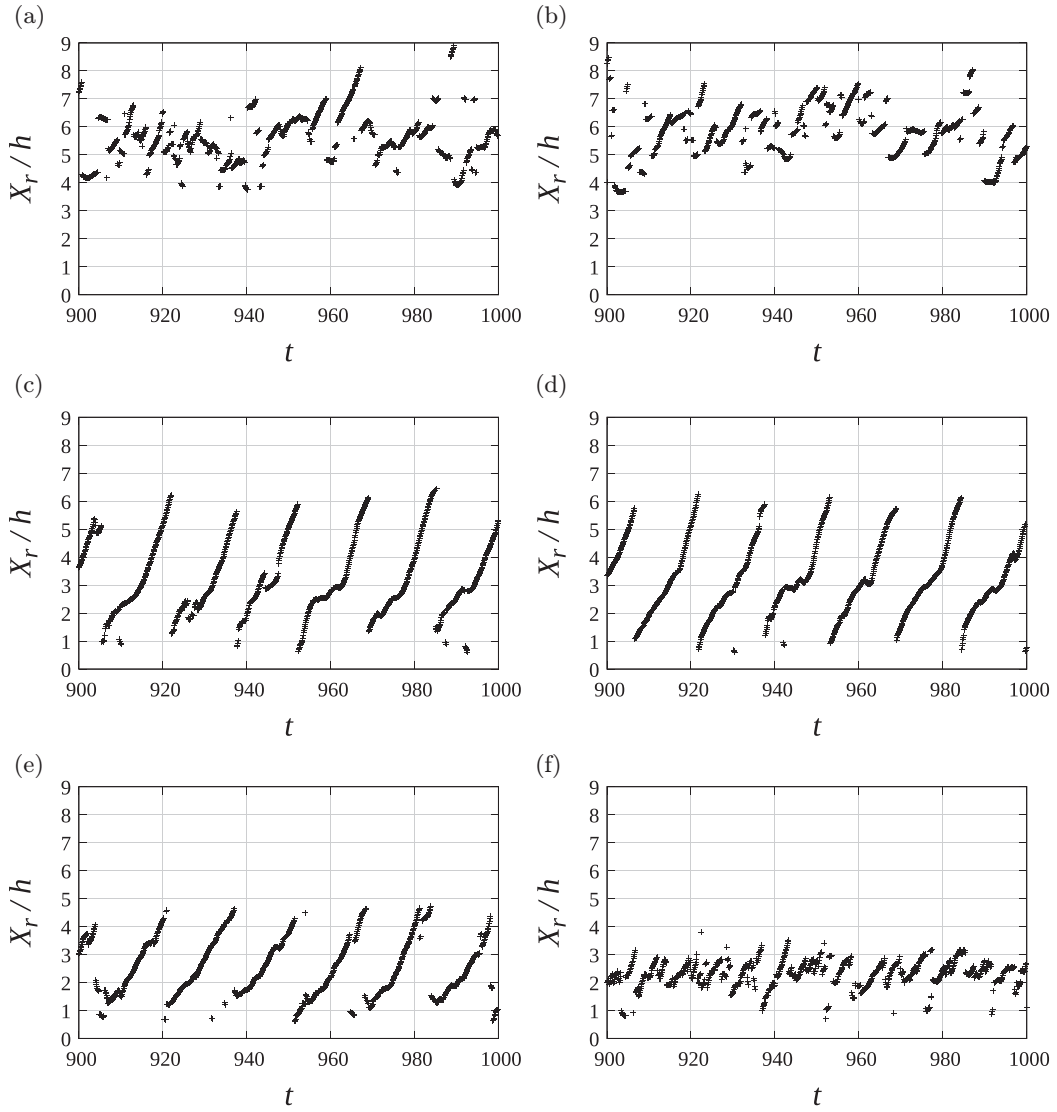

FIG. 15. Time trace of the reattachment length in (a) w/o control, (b) SUTW at $c = 0.4$, and (c) WMTW at $c = 0.4$. Left column is $z = \pi/4$ and right column is $z = \pi/2$.

and wavespeed are the same for WMTW and SUTW, $c = 0.4$ and $\lambda_x = 2\pi$. However, at $\phi_z = \lambda_z/2$, the frequency is doubled, $f = 0.13$, and the oscillation width is significantly smaller than the others. This is because of two reasons: first, the body force is $f_y = 0$ at the nodes (i.e., at $\phi_z = \lambda_z/2$); second, the behavior at $\phi_z = \lambda_z/4$ and $3\lambda_z/4$ are shifted by just half a period $T/2$ and both affect the behavior at $\phi_z = \lambda_z/2$.

Thus, SUTW and WMTW govern the frequency of the reattachment length by periodically repeating the expansion and generation/release of recirculation bubbles. Additionally, the generation/release of the recirculation bubble significantly reduces the reattachment length, which is a common reduction mechanism in both controls.

Figure 17 shows the velocity vector averaged in phase and z direction ($\overline{\langle u \rangle}^z$, $\overline{\langle v \rangle}^z$) in SUTW. Here, only $2\pi \leqslant x \leqslant 4\pi$ and $0 \leqslant y \leqslant 1$ are displayed, and the black object represents the step. The

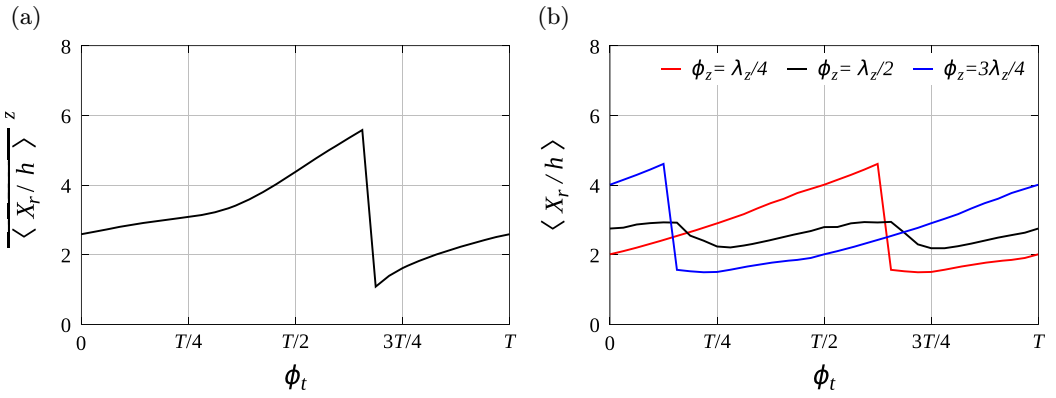

FIG. 16. Phase-averaged reattachment length in (a) SUTW and (b) WMTW.

wall-normal body force distribution applied above the step is shown in the step to aid the reader's understanding. At $\phi_t = 0$, the positive body force generates an upward flow on the step. At $\phi_t = T/4$, the upward flow is transported to the separation point. At $\phi_t = T/2$, the upward flow combines with the recirculation bubble, which increases the size and rotation of the recirculation bubble. The enhanced backflow in the recirculation bubble generates the secondary bubble, which moves the

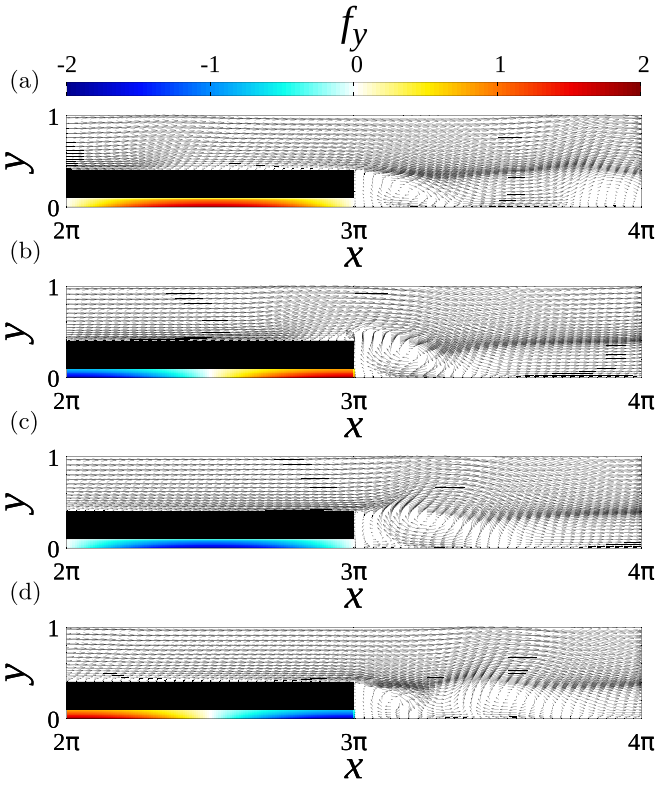

FIG. 17. Velocity vector averaged in phase and z direction ($\overline{\langle u \rangle}^z$, $\overline{\langle v \rangle}^z$) around the separation point in SUTW. The contour shown in the step is wall-normal body force f_y: (a) $\phi_t = 0$; (b) $\phi_t = T/4$; (c) $\phi_t = T/2$; (d) $\phi_t = 3T/4$.

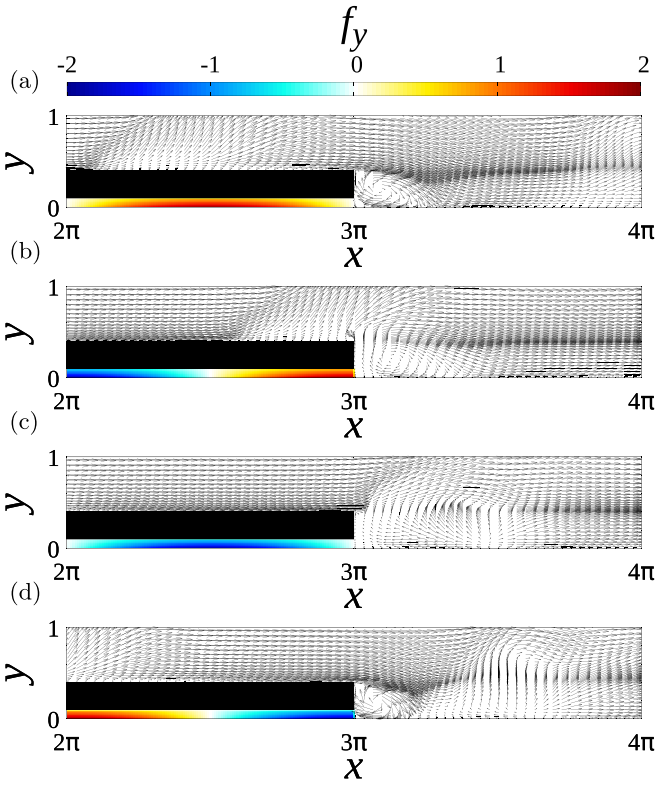

FIG. 18. Phase-averaged velocity vector $(\langle u\rangle, \langle v\rangle)$ around the separation point at $\phi_z = \lambda_z/4$ in WMTW with $c = 0.4$. The contour shown in the step is wall-normal body force f_y: (a) $\phi_t = 0$; (b) $\phi_t = T/4$; (c) $\phi_t = T/2$; (d) $\phi_t = 3T/4$.

recirculation bubble downstream. Conversely, the negative body force generates the downward flow above the step. At $\phi_t = 3T/4$, the downward flow releases the original recirculation bubble and generates a new recirculation bubble.

Figure 18 shows the phase-averaged velocity vector $(\langle u\rangle, \langle v\rangle)$ at $\phi_z = \lambda_z/4$ in WMTW with $c = 0.4$. At $\phi_t = 0$, the positive body force generates significantly strong upward flow on the step. At $\phi_t = T/4$ and $T/2$, the upward flow expands the recirculation bubble as in SUTW, but its rotation is weakened unlike SUTW, which suppresses the formation of secondary bubble. At $\phi_t = 3T/4$, the downward flow generated by the negative body force pushes the recirculation bubble downstream and forms a new bubble as in SUTW. However, near the separation point, the downward flow is stronger than SUTW, which results in a more enhanced rotation of the recirculation bubble.

Figure 19 shows the phase-averaged velocity vector $(\langle u\rangle, \langle v\rangle)$ at $\phi_z = \lambda_z/2$ in WMTW with $c = 0.4$. The body force is always $f_y = 0$. Hence, the flow on the step is relatively constant at any time, and the recirculation bubble oscillates slightly without being released. Compared to the SUTW, the secondary bubble is extremely small, and thereby, it cannot be identified.

In summary, the behavior at $\phi_z = \lambda_z/4$ and $\phi_z = \lambda_z/2$ in WMTW is significantly different because each body force distribution does not coincide at the same time ϕ_t and x-coordinate. Conversely, at $\phi_z = \lambda_z/4$ in WMTW, the effects of body forces on the behavior of the recirculation bubble are very similar to that in SUTW because the periodicity in time and streamwise direction is the same: the positive body forces generate the upward flow above the step, which increases the size of the recirculation bubble; the negative body forces generate the downward flow above the step, which generates and releases the recirculation bubbles. However, there are three different effects.

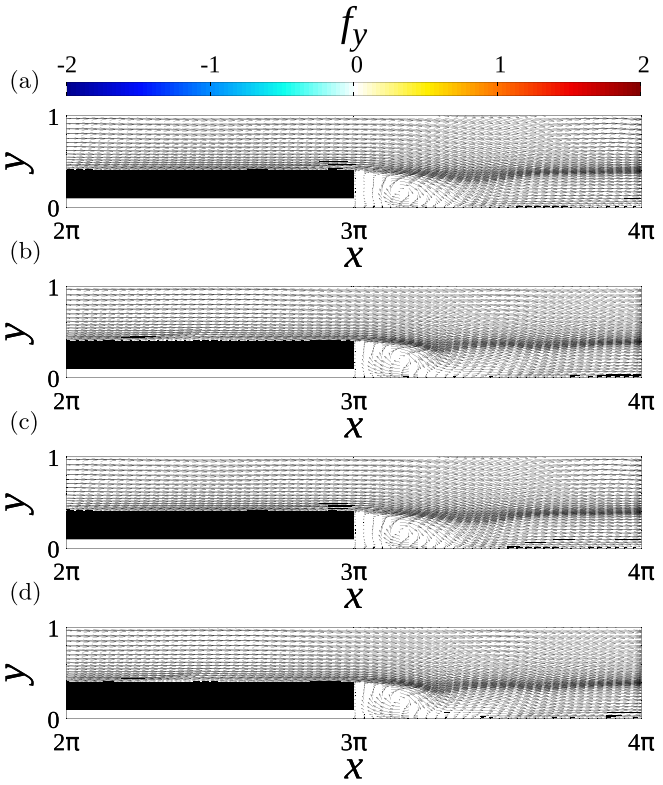

FIG. 19. Phase-averaged velocity vector $(\langle u\rangle, \langle v\rangle)$ around the separation point at $\phi_z = \lambda_z/2$ in WMTW with $c = 0.4$. The contour shown in the step is wall-normal body force f_y: (a) $\phi_t = 0$; (b) $\phi_t = T/4$; (c) $\phi_t = T/2$; (d) $\phi_t = 3T/4$.

First, the upward and downward flows in WMTW are stronger than that in SUTW. This is because of the pair of longitudinal vortices above the step as shown in Fig. 10. Second, the strong downward flow in WMTW generates new recirculation bubbles with more enhanced rotation. Third, in SUTW, the upward flow enhances the rotation of z axis in the recirculation bubble, which produces the secondary bubble, whereas in WMTW, the strong upward flow weakens the z axis rotation in the recirculation bubble, which suppresses the generation of the secondary bubble. This is because of the fact that the dominant rotation axis of the recirculation bubble is in the z direction in SUTW and in the x direction in WMTW, as shown in Fig. 10 and Fig. 12.

Figure 20 shows the phase-averaged velocity vector $(\langle v\rangle, \langle w\rangle)$ and phase-averaged wall-normal velocity $\langle v\rangle$ in WMTW with $c = 0.4$. At separation point $x = 3\pi$, the body force at $\phi_t = 0$ [Fig. 20(a)] is zero. At $\phi_t = T/8$ [Fig. 20(c)], the positive and negative body forces generate the upward and downward flows, respectively. At $\phi_t = T/4$ [Fig. 20(e)], these flows become the pair of longitudinal vortices. At $\phi_t = 3T/8$ [Fig. 20(g)], this pair of longitudinal vortices is maintained but weakens. Accordingly, at the separation point [Figs. 20(a), 20(c), 20(e), and 20(g)], a pair of longitudinal vortices is generated, which enhances the upward and downward flows.

At the reattachment point $x = 10.46$, a pair of longitudinal vortices exist on the right side at $\phi_t = 0$ [Fig. 20(b)]. At $\phi_t = T/8$ and $T/4$ [Figs. 20(d) and 20(f)], this pair of longitudinal vortices is maintained but gradually becomes weak. At $\phi_t = 3T/8$ [Fig. 20(h)], a new pair of longitudinal vortices is generated on the left side. Therefore, this pair of longitudinal vortices is generated alternately at $0 \leqslant z \leqslant \pi/2$ and $\pi/2 \leqslant z \leqslant \pi$ at the reattachment point [Figs. 20(b), 20(d), 20(f), and 20(h)]. As shown in Fig. 12, these longitudinal vortices are the recirculation bubbles whose

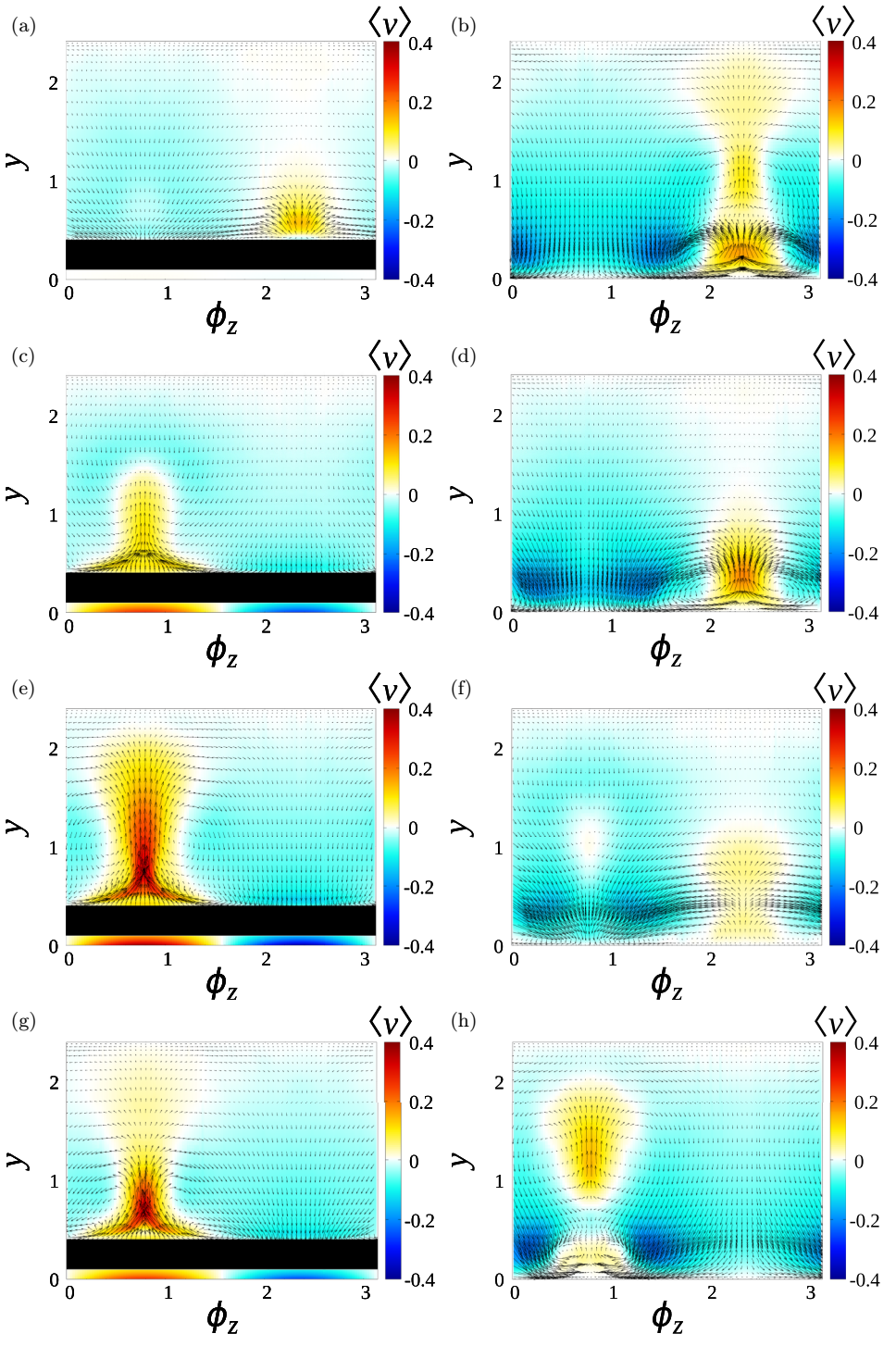

FIG. 20. Phase-averaged velocity vector $(\langle v\rangle, \langle w\rangle)$ and phase-averaged wall-normal velocity $\langle v\rangle$ in WMTW with $c = 0.4$. The contour shown in the step is wall-normal body force f_y. Left column is at the separation point $x = 3\pi$ and right column is at the reattachment length $x = 10.46$: (a, b) $\phi_t = 0$; (c, d) $\phi_t = T/8$; (e, f) $\phi_t = T/4$; (g, h) $\phi_t = 3T/8$.

rotation axis has been changed from the z direction to the x direction. In the released separation bubble, the x-axis rotation becomes the core of the horseshoe vortex.

Thus, WMTW generates a pair of longitudinal vortices above the step and in the separation region. The streamwise rotation in the pair of longitudinal vortices enhances the localized downward flow owing to the synergistic effect of both vortices. Additionally, the presence of rotation in the x direction as well as z direction increases the RSS in WMTW more than that in SUTW. These two effects contribute directly to the reduction of reattachment length.

IV. CONCLUSION

In this study, we performed the DNS of the BFS turbulent flow controlled by the wall-normal body force in the form of a wave-machine-like traveling wave above the step. This control exhibits streamwise and spanwise periodicity, which is expected to increase additional turbulence and further reduce the reattachment length. To analyze the effect of spanwise periodicity, we compared spanwise-uniform traveling waves (SUTW) and wave-machine-like traveling waves (WMTW).

The parametric study showed that the maximum reattachment length reduction rates are 51.4% at $c = 0.4$ (and $\lambda_z = \infty$) for SUTW and 58.9% at $c = 0.4$ and $\lambda_z = \pi$ for WMTW. For these two cases, statistics averaged in time and z direction showed the three advantages of WMTW over SUTW with respect to reattachment length reduction: the decrease in the streamwise length of the secondary bubble; the enhancement of the negative wall-normal velocity; and the increase in RSS.

Analysis based on phase average revealed similarities provided by the same periodicity in time and x direction for SUTW and WMTW, i.e., the effect of body force on the behavior of the recirculation bubble: positive body forces induce upward flow above the step, which increases the size of the recirculation bubble; negative body forces induce downward flow above the step, which generates the new recirculation bubble and releases the original recirculation bubble. Specifically, the periodic generation/release of recirculation bubble contributes significantly to the reattachment length reduction as a common mechanism.

Conversely, the spanwise periodicity produced differences in the flow structure. In SUTW, spanwise-uniform upward and downward flows are induced time-periodically, which lead to the expansion and generation/release of spanwise-uniform recirculation bubble, respectively. In WMTW, the time-periodic behavior is very similar to SUTW, but the spanwise structure is affected by the spanwise phase of the control. Therefore, the upward and downward flows, generated alternately in the spanwise direction, form the pair of longitudinal vortices above the step. Analogously, these flows simultaneously cause the expansion and generation/release, which form the spanwise sinusoidal recirculation bubble. The expanded recirculation bubble grows into a pair of longitudinal vortices. When the recirculation bubble is released, the pair of longitudinal vortices becomes the horseshoe vortex.

Thus, the effect of flow structure in WMTW on reattachment length is clarified. The flow structure above the step, recirculation bubble, and released separation bubble exhibit the shape of a pair of longitudinal vortices. The synergy effect of both longitudinal vortices directly and significantly reduced the negative wall-normal velocity. Additionally, the rotation of the x-axis as well as z-axis increase the turbulence, i.e., RSS. The x-axis rotation weakens the z-axis rotation, which suppresses the formation of the secondary bubble.

ACKNOWLEDGMENT

This study was partially supported by JSPS KAKENHI Grant No. 21K18685 and No. 21H05007.

[1] D. M. Kuehn, Effects of adverse pressure gradient on the incompressible reattaching flow over a rearward-facing step, AIAA J. **18**, 343 (1980).
[2] M. V. Ötügen, Expansion ratio effects on the separated shear layer and reattachment downstream of a backward-facing step, Exp. Fluids **10**, 273 (1991).
[3] B. F. Armaly, F. Durst, J. C. F. Pereira, and B. Schönung, Experimental and theoretical investigation of backward-facing step, J. Fluid Mech. **127**, 473 (1983).
[4] D. M. Driver and H. L. Seegmiller, Features of a reattaching turbulent shear layer in divergent channel flow, AIAA J. **23**, 163 (1985).
[5] P. Bradshaw and F. Y. F. Wong, The reattachment and relaxation of a turbulent shear layer, J. Fluid Mech. **52**, 113 (1972).
[6] H. Le, P. Moin, and J. Kim, Direct numerical simulation of turbulent flow over a backward-facing step, J. Fluid Mech. **330**, 349 (1997).
[7] S. Jovic and D. M. Driver, Backward-facing step measurements at low Reynolds number, $\mathrm{Re}_h = 5000$, *NASA Technical Memorandum* (Ames Research Center, CA, 1994), p. 108807.
[8] M. Barri, G. K. El Khoury, H. I. Andersson, and B. Pettersen, DNS of backward-facing step flow with fully turbulent inflow, Int. J. Numer. Methods Fluids **64**, 777 (2010).
[9] M. Barri, G. K. El Khoury, H. I. Andersson, and B. Pettersen, Inflow conditions for inhomogeneous turbulent flows, Int. J. Numer. Methods Fluids **60**, 227 (2009).
[10] J. Kim, P. Moin, and R. Moser, Turbulence statistics in fully developed channel flow at low Reynolds number, J. Fluid Mech. **177**, 133 (1987).
[11] N. Kasagi and A. Matsunaga, Three-dimensional particle-tracking velocimetry measurement of turbulence statistics and energy budget in a backward-facing step flow, Int. J. Heat Fluid Flow **16**, 477 (1995).
[12] F. Schäfer, M. Breuer, and F. Durst, The dynamics of the transitional flow over a backward-facing step, J. Fluid Mech. **623**, 85 (2009).
[13] G. Biswas, M. Breuer, and F. Durst, Backward-facing step flows for various expansion ratios at low and moderate Reynolds numbers, J. Fluids Eng. **126**, 362 (2004).
[14] A. Pont-Vílchez, F. X. Trias, A. Gorobets, and A. Oliva, Direct numerical simulation of backward-facing step flow at $\mathrm{Re}_\tau = 395$ and expansion ratio 2, J. Fluid Mech. **863**, 341 (2019).
[15] K. B. Chun and H. J. Sung, Control of turbulent separated flow over a backward-facing step by local forcing, Exp. Fluids **21**, 417 (1996).
[16] H. Wengle, A. Huppertz, G. Bärwolff, and G. Janke, The manipulated transitional backward-facing step flow: An experimental and direct numerical simulation investigation, Eur. J. Mech. B Fluids **20**, 25 (2001).
[17] J. A. Dahan, A. S. Morgans, and S. Lardeau, Feedback control for form-drag reduction on a bluff body with a blunt trailing edge, J. Fluid Mech. **704**, 360 (2012).
[18] T. Min, S. M. Kang, J. L. Speyer, and J. Kim, Sustained sub-laminar drag in a fully developed channel flow, J. Fluid Mech. **558**, 309 (2006).
[19] J. Hœpffner and K. Fukagata, Pumping or drag reduction? J. Fluid Mech. **635**, 171 (2009).
[20] C. Lee, T. Min, and J. Kim, Stabillity of a channel flow subject to wall blowing and suction in the form of a traveling wave, Phys. Fluids **20**, 101513 (2008).
[21] H. Mamori, K. Iwamoto, and A. Murata, Effect of the parameters of traveling waves created by blowing and suction on the relaminarization phenomena in fully developed turbulent channel flow, Phys. Fluids **26**, 015101 (2014).
[22] S. Koganezawa, A. Mitsuishi, T. Shimura, K. Iwamoto, H. Mamori, and A. Murata, Pathline analysis of traveling wavy blowing and suction control in turbulent pipe flow for drag reduction, Int. J. Heat Fluid Flow **77**, 388 (2019).
[23] K. Uchino, H. Mamori, and K. Fukagata, Heat transfer in fully developed turbulent channel flow with streamwise traveling wave-like wall deformation, J. Thermal Sci. Technol. **12**, 11 (2017).
[24] R. Yamamoto, J. Morita, H. mamori, T. Miyazaki, and S. Hara, Turbulent channel flow controlled by traveling wave-like body force mimicking oscillating thin films, Phys. Fluids **34**, 085106 (2022).
[25] J. Morita, H. Mamori, and T. Miyazaki, Direct numerical simulation of the backward-facing step turbulent flow controlled by traveling wave-like body force, Int. J. Heat Fluid Flow **95**, 108964 (2022).

[26] H. Mamori and K. Fukagata, Drag reduction effect by a wave-like wall-normal body force in a turbulent channel flow, Phys. Fluids **26**, 862 (2014).
[27] Y. Nabae and K. Fukagata, Drag reduction effect of streamwise traveling wave-like wall deformation with spanwise displacement variation in turbulent channel flow, Flow, Turbul. Combust. **109**, 1175 (2022).
[28] F. H. Harlow and J. E. Welch, Numerical calculation of time-dependent viscous incompressible flow of fluid with free surface, Phys. Fluids **8**, 2182 (1965).
[29] J. Kim, D. Kim, and H. Choi, An immersed-boundary finite-volume method for simulations of flow in complex geometries, J. Comput. Phys. **171**, 132 (2001).
[30] K. Fukagata and N. Kasagi, A theoretical prediction of friction drag reduction in turbulent flow by superhydorophobic surfaces, Phys. Fluids **18**, 051703 (2006).
[31] F. E. Ham, F. S. Lien, and A. B. Strong, A fully conservative second-order finite difference scheme for incompressible flow on nonuniform grids, J. Comput. Phys. **177**, 117 (2002).
[32] J. K. Dukowicz and A. S. Dvinsky, Approximate factorization as a higher-order splitting for the implicit incompressible flow equations, J. Comput. Phys. **102**, 336 (1992).